Metallic Membranes with Subwavelength Complementary Patterns: Distinct Substrates for Surface-Enhanced Raman Scattering

Qingzhen Hao,[†,‡,⊥] Yong Zeng,[§,⊥] Bala Krishna Juluri,[‡] Xiande Wang,[§] Brian Kiraly,[‡] I-Kao Chiang,[‡] Lasse Jensen,[∥] Douglas H. Werner,[§] Vincent H. Crespi,[†] and Tony Jun Huang[‡,*]

[†]Department of Physics, [‡]Department of Engineering Science and Mechanics, [§]Department of Electrical Engineering, and [∥]Department of Chemistry, The Pennsylvania State University, University Park, Pennsylvania 16802, United States. [⊥]These authors contributed equally to this article.

ABSTRACT We present a detailed comparison of surface-enhanced Raman spectroscopy (SERS) signals from metallic nanoparticle arrays and their complementary hole arrays. Using an analytical model for local field enhancement, we show that the SERS enhancements of the hole arrays are closely related to their transmission spectra. This trend is experimentally confirmed and characterized by a $\cos^4\theta$ dependence of the SERS signal on the excitation polarization angle θ. The particle arrays, on the other hand, exhibit quite different behavior because of the existence of considerable evanescent modes in the near field. Their maximal local field gains appear at wavelengths generally much larger than their localized surface plasmonic resonant wavelengths.

KEYWORDS: complementary · SERS · nanostructure · near field · nanoparticle · nanohole

Since its discovery in the 1970s,[1,2] surface-enhanced Raman scattering (SERS) has attracted a great deal of attention in the chemistry, physics, materials science, and life science communities (see ref 3 and the references therein). A combination of metal-molecule chemical effects and intense enhancement of localized electromagnetic fields around metallic nanostructures[4,5] can increase the cross section of Raman scattering, matching or even exceeding that of linear Rayleigh scattering.[6−9] A wealth of SERS substrates have been introduced, such as arrays of metallic nanoparticles or thin metallic films with subwavelength patterns.[10−20]

According to Babinet's principle,[21] an array of metallic nanoparticles and the complementary array of holes have nearly complementary linear optical spectra under illumination with parallel and transverse polarizations, respectively. In fact, maximal transmission in the hole array occurs nearly at the position for the extinction peak of the complementary particle array, as confirmed by our recent experimental study.[22] In this work, we present a detailed comparison of the SERS signals from gold nanoparticle arrays and their complementary hole arrays. Using an analytical model for the local field enhancement, we show that the SERS enhancements of the hole arrays are closely related to their transmission spectra. This trend is confirmed experimentally and characterized by a $\cos^4\theta$ dependence of the SERS signal on the excitation polarization angle θ. The particle arrays, on the other hand, exhibit quite different behavior because of the existence of considerable evanescent modes in the near field. Their maximal local field gains appear at wavelengths generally much larger than their localized surface plasmonic resonant wavelengths.

RESULTS AND DISCUSSION

Several enhancement mechanisms are generally involved in SERS. Here we concentrate exclusively on the electromagnetic enhancement mechanism.[23−26] Note that the complementary structures have very different mechanisms for enhancing the local electromagnetic field. Localized surface plasmonic resonances (LSPRs) are usually excited for particle arrays, and these resonances will result in strong reflections.[22,27−32] The underlying physics of subwavelength hole arrays in metallic membranes, on the other hand, is quite complicated and generally involves localized or propagating surface plasmons and waveguide modes.[33−35] To simplify the notation in this paper, we will name all these different mechanisms uniformly as shape resonances and denote the corresponding wavelengths as λ_{sr}.

* Address correspondence to junhuang@psu.edu.

Received for review February 21, 2011 and accepted June 9, 2011.

Published online June 09, 2011
10.1021/nn200704p

To measure the degree of local field enhancement, we define a local field gain $g(\omega,\mathbf{x})$ as[36]

$$g(\omega,\mathbf{x}) = \left|\frac{E_l(\omega,\mathbf{x})}{E_{ex}(\omega,\mathbf{x})}\right|^2 \quad (1)$$

with E_l and E_{ex} being the local field and the external excitation field, respectively. Ignoring any polarization/surface selection rule effects, the SERS enhancement $G(\omega_{ex},\mathbf{x})$ is approximated to be $g(\omega_{ex},\mathbf{x})\ g(\omega_r,\mathbf{x})$, with ω_{ex} and ω_r representing the excitation and the corresponding Raman frequency, respectively.[3] Further assuming the molecules are uniformly distributed on the surface of the array, we can define an averaged function $f_a(\omega)$ to characterize the optical properties of the substrate.

$$f_a(\omega) = \frac{1}{d^2}\int_{-d/2}^{d/2} dx \int_{-d/2}^{d/2} dy f(\omega,\mathbf{x}) \quad (2)$$

where d is the lattice spacing of the array, $\mathbf{x} = (x,y,0^-)$, and f_a can be either g_a or G_a. Moreover, we denote the position of maximal g_a and G_a as λ_{lc} and λ_{rm}, respectively. Generally λ_{rm} should be on the higher energy side of λ_{lc}.[3]

To estimate the local field enhancement g, we consider a free-standing structure consisting of a square lattice of metallic elliptical particles arranged in the xy plane (note that the following analysis can be extended to hole arrays as well). The two axes of the elliptical particles and the two primitive vectors of the square lattice are assigned to be parallel to the x and y directions, respectively; see Figure 2d. The substrate therefore has two planes of mirror symmetry. The incident plane wave is further assumed to be $e^{ik_0 z}\mathbf{e}_x$, with $k_0 = 2\pi/\lambda$ being the free-space wavenumber and λ being the excitation wavelength. Consequently the polarization current inside the metal obeys the following symmetry properties:

$$\begin{aligned} J_x(x,y) &= J_x(x,\ -y),\ J_y(x,y) \\ &= -J_y(x,\ -y),\ J_z(x,y) = -J_z(x,\ -y) \end{aligned} \quad (3)$$

The resultant scattering electric field can be expressed in the form

$$\begin{aligned} \mathbf{E}(\mathbf{x}) = \sum_{mn} \frac{-Z_0\lambda S_{mn}}{4\pi k_{mn} d^2} e^{i\mathbf{k}_{mn}\cdot\mathbf{x}} \Big[(k_{mn,y}^2 + k_{mn,z}^2)\mathbf{e}_x \\ - k_{mn,x}k_{mn,y}\mathbf{e}_y - k_{mn,x}k_{mn,z}\mathbf{e}_z\Big] \end{aligned} \quad (4)$$

with $Z_0 = (\mu_0/\varepsilon_0)^{1/2}$ being the free-space intrinsic impedance. The wave vector of the (m,n)-order scattered wave is given by

$$\begin{aligned} \mathbf{k}_{mn} &= mk_d\mathbf{e}_x + nk_d\mathbf{e}_y \pm \kappa_{mn}\mathbf{e}_z, \\ \kappa_{mn} &= \sqrt{k_0^2 - k_d^2(m^2+n^2)} \end{aligned} \quad (5)$$

with $k_d = 2\pi/d$. The positive sign of κ_{mn} corresponds to forward scattering, or a transmitted wave, and the negative sign represents backward scattering, or a reflected wave. Moreover, the contribution from one unit cell of the substrate can be written as

$$\begin{aligned} S_{mn} = 4\int_0^{d/2} dy' \int_0^{d/2} dx' \int_0^h dz' J_x e^{-ik_{mn,z}z'} \\ \cos(mk_d x')\cos(nk_d y') \end{aligned} \quad (6)$$

with h being the thickness of the metallic film.

Notice that the lattice constant d of our samples is about one-half of the excitation wavelength λ, which results in $\kappa_{00} = k_0$ for the zero-order wave and $\kappa_{mn} \approx ik_d(m^2+n^2)^{1/2}$ for all higher order waves. Under these conditions the function $e^{-ik_{mn,z}z'}$ that appears in the integrand of eq 6 is an exponentially decaying function of z' when m or n is not zero. As a result, the current close to the $z = 0^-$ plane contributes significantly to the non-zero-order S_{mn} of the reflected wave, while the current near the $z = h$ plane can be neglected. This effect will result in a remarkable difference between the near field and far field.[36−38] Because the current distribution inside the metal is strongly affected by the imaginary part of its permittivity, we can imagine an effective substrate with a larger Im ε and hence a smaller skin depth to qualitatively estimate the difference between the near and far field. We would expect the wavelength of the maximal g_a to be longer than the shape resonant wavelength λ_{sr}, because a larger value of Im ε implies a longer wavelength for gold in the optical regime.[39] This red shift of the maximal g_a has been found numerically for a gold sphere as well as an array of cylindrical gold particles.[38]

As a rough approximation, we assume the local fields at the $z = 0^-$ plane are dominated by the combined zero- and first-order scattering waves. The zero-order wave reads as

$$\mathbf{E}^{(0)} = -\frac{Z_0}{2d^2}S_{00}\mathbf{e}_x \equiv r\mathbf{e}_x \quad (7)$$

where r represents the classical Fresnel reflection coefficient. The first-order wave, including $(\pm1,0)$ and $(0,\pm1)$ waves, can be approximated as

$$\mathbf{E}^{(1)} \approx -\frac{Z_0}{2d^2}\frac{i2\lambda}{d}\Big[\cos(k_d x)\mathbf{e}_x + \sin(k_d x)\mathbf{e}_z\Big]S_{10} \quad (8)$$

Notice that the factor $2\lambda/d$ can be much larger than unity for substrates that contain subwavelength patterns. Furthermore, the transverse dimensions of the substrate's unit cell may have a profound influence on S_{10}. To demonstrate this, we assume the current inside the metal is a slowly varying function of x', which nearly holds in the electrostatics regime. Note that the domain of the function $\cos(k_d x')$ that appears in the integrand of eq 6 spans the range nearly from 0 to $d/2$ for the hole structure. The corresponding integration therefore contributes to S_{10} destructively, which further results in a negligible first-order wave. Similar arguments can be extended to higher order S_{mn} terms

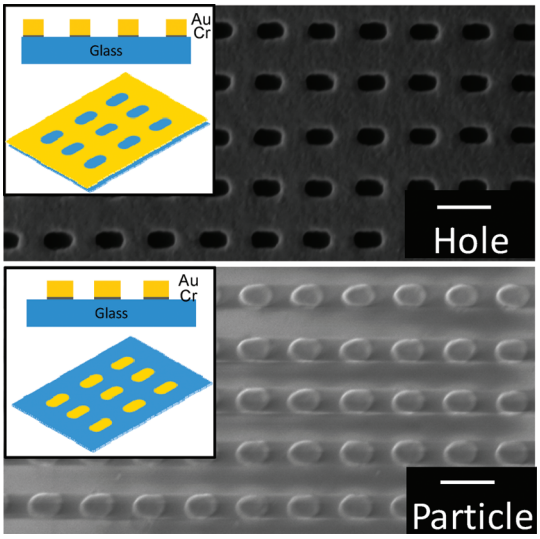

Figure 1. Scanning electron microscope (SEM) images of one set of complements. The major axis of the particle/hole is 180 nm, and the minor axis is 120 nm. Scale bar represents 300 nm. Schematic of the sample is shown in the inset. 1 nm chromium is used as an adhesion layer.

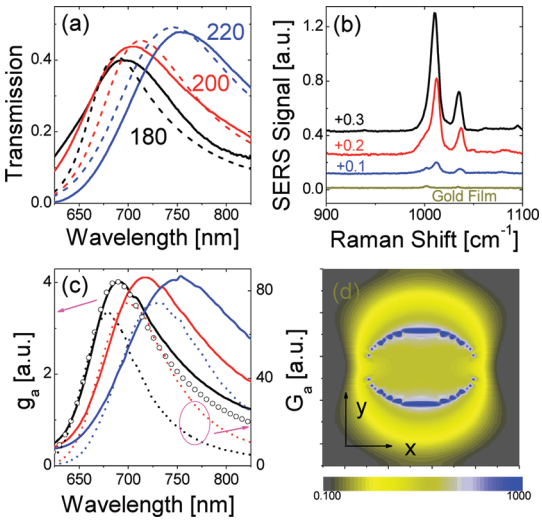

Figure 2. (a) Experimentally measured (solid) and numerically simulated (dashed) transmission spectra for three different hole arrays. (b) SERS signals from the hole arrays and the nonperforated gold film. The curves have been shifted vertically for the sake of clarity. (c) Numerically simulated averaged local field gain $g_a(\omega)$ (solid) as well as SERS enhancement $G_a(\omega)$ (dotted) as a function of the excitation wavelength. Both $g_a(\omega)$ and $G_a(\omega)$ are calculated at $z = 0^-$. The transmission spectrum of the 180 nm hole array is also plotted (open circles). (d) Spatial distribution, on a logarithmic scale, of the SERS enhancement G for the 180 nm hole array. The excitation laser is 647 nm and y-polarized.

for hole arrays. Therefore, the resulting local fields are characterized by the zero-order wave exclusively. By adding the external illumination field, we can write the total local field as $r\mathbf{e}_x + \mathbf{e}_x \approx t\mathbf{e}_x$, where t represents the transmission coefficient.[35] The approximation is valid because (1) the wavelength of the normally incident light is much larger than d as well as (2) the thickness h is much smaller than λ so that retardation effects can be neglected.[40] As a result, *the local field gain will be closely related to the linear transmittance* $|t(\omega)|^2$.

We fabricate three sets of complements, *i.e.*, arrays of subwavelength gold particles and subwavelength holes in thin gold films. One set of complements is shown in Figure 1. The unit cells are arranged in square lattices with a lattice constant of 320 nm. The constituent particle is an elliptical cylinder, with a minor axis of 120 nm, a thickness of 70 nm, and a variable-length major axis. Details regarding the fabrication can be found in ref 22.

Figure 2 summarizes our results regarding the subwavelength hole arrays. In all the measurements, the incident plane waves are y-polarized and propagate along the z direction. The measured transmission spectra are plotted in Figure 2a with solid curves. We observe that the larger the semimajor axis of the elliptical hole, the longer the resonant wavelength for the array, in agreement with our previous results.[22] Using a hybrid finite-element boundary-integral method, we numerically calculated the linear spectra of these hole arrays in air (see ref 41 for more details). The nanoholes are elliptical cylinders with a mesh size of 4 nm. Only one unit cell is needed in the simulation since periodic boundary conditions have been employed. Moreover, the refractive index used for gold is identical to the experimental measurements reported in ref 42, and the glass substrate is assumed to be infinitely thick for computational efficiency. The numerical results, plotted with a dashed curve, are found to be in reasonable agreement with the experimental results. We further calculate the averaged local field gain, g_a, as well as the averaged SERS enhancement, G_a, on a plane 1 nm above the metal−air interface. (Note that this does not exactly reflect experiments where molecules are expected to coat all the surface of nanoholes. However, numerical simulations have shown that this is qualitatively valid.). The results are depicted in Figure 2c with solid and dotted curves, respectively. As a reference, we also plot the transmission spectra of the 180 nm hole array. Consistent with the theory above, the local gains g_a are nearly proportional to the corresponding transmission spectra at a given wavelength for all three structures, and the wavelength of maximal g_a is found to slightly red-shift with respect to that of the maximal transmission. Furthermore, the calculated SERS enhancement G_a has a curve quite similar to that of g_a^2, with a narrower bandwidth. The excitation wavelength of the maximal G_a, λ_{rm}, sits on the higher energy side of the λ_{lc}. The reason for this blue shift is that an enhanced SERS requires us to increase both local field gains at the excitation wavelength and the corresponding Raman wavelength.

Using pyridine as a probing molecule and an excitation wavelength of 647 nm, we measured Raman scattering from the three hole arrays as well as a nonperforated gold film. (Note that the Raman measurement

was done with aqueous pyridine solution, and the small resonance shift induced by water does not alter our observations qualitatively. Please see more discussions about the medium effect in the Methods part.) The results are plotted in Figure 2b. All three arrays provide Raman signals much stronger than that from the gold film. The strongest Raman signal results from the 180 nm sample, in good agreement with the numerical predications. At this excitation wavelength, the 220 nm hole array is found to have the smallest G_a, although we can interpret the results with the empirical rule: the closer the excitation wavelength to the shape resonance λ_{sr}, the stronger the Raman signal. We argue here that a better explanation relies on the transmittance around the excitation wavelength, if we take into account the relation $\lambda_{rm} \approx \lambda_{sr} - \Delta/2$, with Δ being the Raman shift.

To further explore the strong correlation between the transmission of the subwavelength hole array and its SERS enhancement, we studied the effect of the excitation polarization angle θ on the Raman signal of the 180 nm hole array. Both experimental (square) and numerical (dot) results are plotted in Figure 3. It is found that the *y*-polarized excitation provides the strongest Raman signal, whereas the *x*-polarized illumination leads to the weakest signal. To interpret the dependence, we first recall that the dependence of the transmittance $|t|^2$ on the polarization angle can be described as

$$|t|^2(\theta) = |t|^2(0)\cos^2\theta + |t|^2(\pi/2)\sin^2\theta \qquad (9)$$

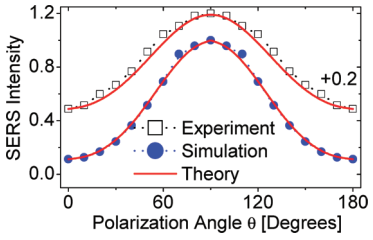

Figure 3. Dependence of the SERS intensity of pyridine for the 180 nm hole array on the incident polarization angle θ. The angle $\theta = 90^\circ$ (0) corresponds to vertical (horizontal) polarization. The theoretical curves are obtained from eq 10. The set of experimental measurements has been shifted vertically.

as found in our previous paper.[22] By using the fact that g_a is nearly proportional to $|t|^2$ at a given wavelength and further assuming $g(\omega_{ex}) \approx g(\omega_r)$, the SERS enhancement can be approximated as

$$G_a(\theta) \approx G_a(0)\cos^4\theta + G_a(\pi/2)\sin^4\theta + 2\sqrt{G_a(0)\,G_a(\pi/2)}\cos^2\theta\sin^2\theta \qquad (10)$$

with $G_a(0)$ and $G_a(\pi/2)$ being the enhancement factors corresponding to the 647 nm illumination with polarization angles of zero or $\pi/2$, respectively. This equation is then used to fit the experimental measurements as well as the simulations. As shown in Figure 3, the results from eq 10 are in excellent agreement with both the experiments and the numerical simulations. This shows that the local field enhancement g_a of the subwavelength hole array follows the same polarization dependence as its far-field transmission $|t|^2$ and is consistent with that fact that g_a is closely related to $|t|^2$.

Using two different excitation wavelengths, we studied SERS from the complementary particle arrays. The results are presented in Figure 4. Because their characteristic sizes are considerably smaller than the lattice spacing *d*, the cosine function in eq 6 will be positive over nearly the entire integration region, which then constructively contributes to S_{10}. Therefore, there will be a significant contribution to the near field from the first-order scattering waves. Similarly, all the higher order scattering waves are found to exhibit strong local field enhancements. These considerable near-field modes lead to a significant red shift of λ_{lc} with respect to λ_{sr}; the particle arrays therefore exhibit SERS behavior that is quite different from their far-field spectra. This is exactly what we observed: the maximal G_a of the 180 nm particle is found around 740 nm wavelength, much larger than 681 nm, its plasmonic resonant wavelength. Consequently, illuminated by the 647 nm laser, the SERS enhancement of the 180 nm particle array is much smaller than that of its complementary counterpart. When the laser wavelength is tuned to 785 nm, the particle however emits much stronger Raman signals than that of its complement. We also estimate the SERS enhancement factor for the complementary structures under 647 nm excitation

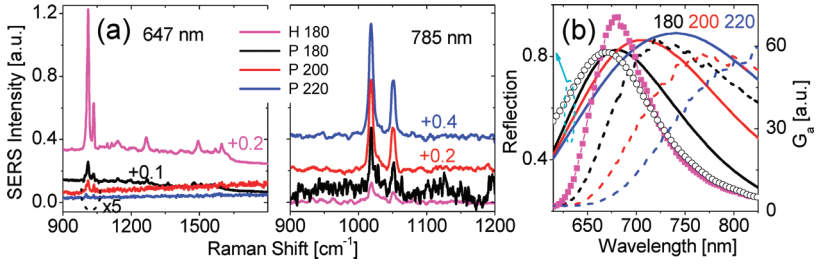

Figure 4. (a) Experimentally measured SERS signals from a 180 nm hole array as well as its complementary particle array. The incident polarizations are also complementary. The wavelength of the laser is set to be 647 and 785 nm, respectively. Note that the curves have been shifted vertically for the sake of clarity. (b) Numerically simulated reflection spectra (solid) and the SERS enhancement G_a (dashed) of the particle arrays. As a reference, the G_a (squares) of the 180 nm hole array is plotted. Note that $G_a(\omega)$ is calculated at $z = 0^-$. The experimentally measured reflection of the 180 nm particle array (circles) is plotted.

(see ref 43 for more details). For the 180 nm hole array, this factor is around 4×10^5, and the particle array gives an enhancement factor of about 5×10^4. On the other hand, a meaningful polarization study could not be carried out on the particle array because the SERS signals are too weak. In general, a $\cos^4 \theta$ is expected for polarized detection along the same direction as the excitation direction, but a $\cos^2 \theta$ is expected for unpolarized detection.[44–47]

SUMMARY

In summary, we performed a comprehensive study of SERS from subwavelength arrays of gold nanoparticles as well as their complementary hole arrays. We show that the averaged local field gains and the SERS enhancements of the hole arrays are strongly correlated to their transmission spectra, and the dependence of the Raman intensities on the excitation polarization angle θ can be approximately described by a $\cos^4 \theta$ model. The complementary particle arrays, on the other hand, present maximal local field gains at wavelengths generally much longer than their localized surface plasmonic resonant wavelengths due to the nontrivial evanescent mode contribution to the near field. We believe the observed differences will serve as useful guidelines for the design of SERS substrates.

METHODS

Measurement and Instruments. Using a deuterium-tungsten light source, we measure the linear optical spectra of the complementary structures in air with an Ocean Optics spectrometer (HR4000 CG-UV-NIR). All spectra are collected using a 50× objective with a numerical aperture of 0.5.

The experimental SERS data are collected using an optical cell containing the SERS substrate covered with 0.01 M pyridine (EMD) in 0.1 M KCl aqueous solution (EMD). The SERS substrate is preincubated in pure pyridine solution for one day before transferring to the chemical cell to ensure monolayer coverage. A microscope coverslip is added to the top as a thin window in such a way that the cell is completely filled with pyridine solution. Raman spectra (backscattering geometry) are taken using a Renishaw Invia MicroRaman spectrometer. A 50× objective sampling of about a 1 μm × 1 μm area is used for both hole and particle arrays. For polarization-dependent measurement, a half-wave plate is inserted in the excitation/collection path of the spectrometer. In other words, Raman signals are detected along the same polarization direction as the excitation laser.

The experimental measurements and numerical simulations of the linear spectra for the nanostructures were carried out in air, but SERS measurement was done in aqueous pyridine solution. The different mediums involved do not alter the conclusions. It was observed that by changing the medium from air to water, the LSPRs red-shift about 25 nm (typical spectra from a nanohole sample are shown in Figure 5a). This slight shift does not significantly alter the SERS results because of the specific laser wavelength we employed. An additional SERS measurement with substrates exposed to pyridine vapor, sealed in a chemical cell, has also been carried out. (Note that pyridine is toxic and it is dangerous to handle pyridine vapor.) The result, shown in Figure 5b, is consistent with the case when an aqueous pyridine solution was used.

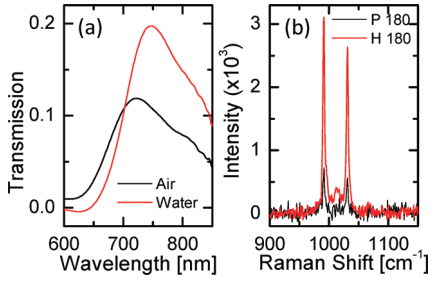

Figure 5. (a) Experimentally measured transmission spectra for a nanohole array with air or water surroundings. (b) SERS measurement of pyridine on the 180 nm complementary nanohole (H 180) and nanoparticle (P 180) arrays.

Acknowledgment. We gratefully acknowledge the financial support from the Air Force Office of Scientific Research (AFOSR), National Science Foundation (NSF), Army Research Office (ARO), and the Penn State Center for Nanoscale Science (MRSEC). Components of this work were conducted at the Penn State node of the NSF-funded National Nanotechnology Infrastructure Network (NNIN).

REFERENCES AND NOTES

1. Fleischm, M.; Hendra, P. J.; Mcquilla, A. J. Raman-Spectra of Pyridine Adsorbed at a Silver Electrode. *Chem. Phys. Lett.* **1974**, *26*, 163–166.
2. Jeanmaire, D. L.; Vanduyne, R. P. Surface Raman Spectroelectrochemistry 0.1. Heterocyclic, Aromatic, and Aliphatic-Amines Adsorbed on Anodized Silver Electrode. *J. Electroanal. Chem.* **1977**, *84*, 1–20.
3. Le Ru, E. C.; Etchegoin, P. G. *Principles of Surface-Enhanced Raman Spectroscopy: And Related Plasmonic Effects*; Elsevier: Amsterdam, 2009.
4. Lombardi, J. R.; Birke, R. L. A Unified Approach to Surface-Enhanced Raman Spectroscopy. *J. Phys. Chem. C* **2008**, *112*, 5605–5617.
5. Jensen, L.; Aikens, C. M.; Schatz, G. C. Electronic Structure Methods for Studying Surface-Enhanced Raman Scattering. *Chem. Soc. Rev.* **2008**, *37*, 1061–1073.
6. Nie, S. M.; Emery, S. R. Probing Single Molecules and Single Nanoparticles by Surface-Enhanced Raman Scattering. *Science* **1997**, *275*, 1102–1106.
7. Li, J. F.; Huang, Y. F.; Ding, Y.; Yang, Z. L.; Li, S. B.; Zhou, X. S.; Fan, F. R.; Zhang, W.; Zhou, Z. Y.; Wu, D. Y.; *et al*. Shell-Isolated Nanoparticle-Enhanced Raman Spectroscopy. *Nature* **2010**, *464*, 392–395.
8. Kodali, A. K.; Llora, X.; Bhargava, R. Optimally Designed Nanolayered Metal-Dielectric Particles as Probes for Massively Multiplexed and Ultrasensitive Molecular Assays. *Proc. Nat. Acad. Sci. U. S. A.* **2010**, *107*, 13620–13625.
9. Li, Z. Y.; Xia, Y. N. Metal Nanoparticles with Gain toward Single-Molecule Detection by Surface-Enhanced Raman Scattering. *Nano Lett.* **2010**, *10*, 243–249.
10. Félidj, N.; Aubard, J.; Levi, G.; Krenn, J. R.; Hohenau, A.; Schider, G.; Leitner, A.; Aussenegg, F. R. Optimized Surface-Enhanced Raman Scattering on Gold Nanoparticle Arrays. *Appl. Phys. Lett.* **2003**, *82*, 3095–3097.
11. Talley, C. E.; Jackson, J. B.; Oubre, C.; Grady, N. K.; Hollars, C. W.; Lane, S. M.; Huser, T. R.; Nordlander, P.; Halas, N. J. Surface-Enhanced Raman Scattering from Individual Au Nanoparticles and Nanoparticle Dimer Substrates. *Nano Lett.* **2005**, *5*, 1569–1574.
12. Brolo, A. G.; Arctander, E.; Gordon, R.; Leathem, B.; Kavanagh, K. L. Nanohole-Enhanced Raman Scattering. *Nano Lett.* **2004**, *4*, 2015–2018.

13. McFarland, A. D.; Young, M. A.; Dieringer, J. A.; Van Duyne, R. P. Wavelength-Scanned Surface-Enhanced Raman Excitation Spectroscopy. *J. Phys. Chem. B* **2005**, *109*, 11279–11285.
14. Reilly, T. H.; Chang, S. H.; Corbman, J. D.; Schatz, G. C.; Rowlen, K. L. Quantitative Evaluation of Plasmon Enhanced Raman Scattering from Nanoaperture Arrays. *J. Phys. Chem. C* **2007**, *111*, 1689–1694.
15. Lesuffleur, A.; Kumar, L. K. S.; Brolo, A. G.; Kavanagh, K. L.; Gordon, R. Apex-Enhanced Raman Spectroscopy Using Double-Hole Arrays in a Gold Film. *J. Phys. Chem. C* **2007**, *111*, 2347–2350.
16. Yu, Q. M.; Guan, P.; Qin, D.; Golden, G.; Wallace, P. M. Inverted Size-Dependence of Surface-Enhanced Raman Scattering on Gold Nanohole and Nanodisk Arrays. *Nano Lett.* **2008**, *8*, 1923–1928.
17. Bahns, J. T.; Guo, Q. T.; Montgomery, J. M.; Gray, S. K.; Jaeger, H. M.; Chen, L. H. High-Fidelity Nano-Hole-Enhanced Raman Spectroscopy. *J. Phys. Chem. C* **2009**, *113*, 11190–11197.
18. Kim, N. H.; Lee, S. J.; Moskovits, M. Aptamer-Mediated Surface-Enhanced Raman Spectroscopy Intensity Amplification. *Nano Lett.* **2010**, *10*, 4181–4185.
19. Gunnarsson, L.; Bjerneld, E. J.; Xu, H.; Petronis, S.; Kasemo, B.; Kall, M. Interparticle Coupling Effects in Nanofabricated Substrates for Surface-Enhanced Raman Scattering. *Appl. Phys. Lett.* **2001**, *78*, 802–804.
20. Wei, H.; Hakanson, U.; Yang, Z. L.; Hook, F.; Xu, H. X. Individual Nanometer Hole-Particle Pairs for Surface-Enhanced Raman Scattering. *Small* **2008**, *4*, 1296–1300.
21. Jackson, J. D. *Classical Electrodynamics*; Wiley: New York, 1999.
22. Hao, Q.; Yong, Z.; Wang, X.; Zhao, Y.; Wang, B.; Werner, D. H.; Crespi, V.; Huang, T. J. Characterization of Complementary Patterned Metallic Membranes Fabricated Simultaneously by a Dual Fabrication Process. *Appl. Phys. Lett.* **2010**, *97*, 193101.
23. Moskovits, M. Surface-Enhanced Spectroscopy. *Rev. Mod. Phys.* **1985**, *57*, 783–826.
24. Kneipp, K.; Moskovits, M.; Kneipp, H. *Surface-Enhanced Raman Scattering: Physics and Applications*; Springer: Berlin, 2006; pp 19–45.
25. Xu, H. X.; Bjerneld, E. J.; Kall, M.; Borjesson, L. Spectroscopy of Single Hemoglobin Molecules by Surface Enhanced Raman Scattering. *Phys. Rev. Lett.* **1999**, *83*, 4357–4360.
26. Xu, H. X.; Aizpurua, J.; Kall, M.; Apell, P. Electromagnetic Contributions to Single-Molecule Sensitivity in Surface-Enhanced Raman Scattering. *Phys. Rev. E* **2000**, *62*, 4318–4324.
27. Lassiter, J. B.; Knight, M. W.; Mirin, N. A.; Halas, N. J. Reshaping the Plasmonic Properties of an Individual Nanoparticle. *Nano Lett.* **2009**, *9*, 4326–4332.
28. Cang, H.; Labno, A.; Lu, C. G.; Yin, X. B.; Liu, M.; Gladden, C.; Liu, Y. M.; Zhang, X. Probing the Electromagnetic Field of a 15-Nanometre Hotspot by Single Molecule Imaging. *Nature* **2011**, *469*, 385–389.
29. Zayats, A. V.; Smolyaninov, I. I.; Maradudin, A. A. Nano-Optics of Surface Plasmon Polaritons. *Phys. Rep.* **2005**, *408*, 131–314.
30. Liu, Y. J.; Hao, Q.; Smalley, J. S. T.; Liou, J.; Khoo, I. C.; Huang, T. J. A Frequency-Addressed Plasmonic Switch Based on Dual-Frequency Liquid Crystals. *Appl. Phys. Lett.* **2010**, *97*, 091101.
31. Zheng, Y. B.; Juluri, B. K.; Mao, X. L.; Walker, T. R.; Huang, T. J. Systematic Investigation of Localized Surface Plasmon Resonance of Long-Range Ordered Au Nanodisk Arrays. *J. Appl. Phys.* **2008**, *103*, 014308–014316.
32. Zheng, Y. B.; Huang, T. J.; Desai, A. Y.; Wang, S. J.; Tan, L. K.; Gao, H.; Huan, A. C. H. Thermal Behavior of Localized Surface Plasmon Resonance of Au/TiO_2 Core/Shell Nanoparticle Arrays. *Appl. Phys. Lett.* **2007**, *90*, 183117.
33. Hao, Q.; Zhao, Y. H.; Juluri, B. K.; Kiraly, B.; Liou, J.; Khoo, I. C.; Huang, T. J. Frequency-Addressed Tunable Transmission in Optically Thin Metallic Nanohole Arrays with Dual-Frequency Liquid Crystals. *J. Appl. Phys.* **2011**, *109*, 084340.
34. Zeng, Y.; Fu, Y.; Chen, X. S.; Lu, W.; Agren, H. Selective Excitation of Surface-Polariton Bloch Waves for Efficient Transmission of Light Through a Subwavelength Hole Array in a Thin Metal Film. *Phys. Rev. B* **2007**, *76*, 035427–035431.
35. García de Abajo, F. J. Colloquium: Light Scattering by Particle and Hole Arrays. *Rev. Mod. Phys.* **2007**, *79*, 1267–1290.
36. Grimault, A. S.; Vial, A.; De La Chapelle, M. L. Modeling of Regular Gold Nanostructures Arrays for SERS Applications Using a 3D FDTD Method. *Appl. Phys. B: Laser Opt.* **2006**, *84*, 111–115.
37. Bryant, G. W.; García de Abajo, F. J. G.; Aizpurua, J. Mapping the Plasmon Resonances of Metallic Nanoantennas. *Nano Lett.* **2008**, *8*, 631–636.
38. Giannini, V.; Vecchi, G.; Rivas, J. G. Lighting Up Multipolar Surface Plasmon Polaritons by Collective Resonances in Arrays of Nanoantennas. *Phys. Rev. Lett.* **2010**, *105*, 266801–266804.
39. Zuloaga, J.; Nordlander, P. On the Energy Shift between Near-Field and Far-Field Peak Intensities in Localized Plasmon Systems. *Nano Lett.* **2011**, *11*, 1280–1283.
40. Zeng, Y.; Moloney, J. V. Volume Electric Dipole Origin of Second-Harmonic Generation from Metallic Membrane with Noncentrosymmetric Patterns. *Opt. Lett.* **2009**, *34*, 2844–2846.
41. Wang, X.; Werner, D. H., Kwon, D.-H. Acceleration of Periodic FEBI Simulations for General Bi-Anisotropic Media using a Model-Based Parameter Estimation Technique. *Proc. IEEE Antennas Propag. Soc. Int. Symp.* San Diego, CA, USA, 2008.
42. Palik, E. D. *Handbook of Optical Constants of Solids*; Academic: New York, 1985.
43. Hao, Q.; Juluri, B. K.; Zheng, Y. B.; Wang, B.; Chiang, I. K.; Jensen, L.; Crespi, V.; Eklund, P. C.; Huang, T. J. Effects of Intrinsic Fano Interference on Surface Enhanced Raman Spectroscopy: Comparison between Platinum and Gold. *J. Phys. Chem. C* **2010**, *114*, 18059–18066.
44. Chen, G.; Wu, J.; Lu, Q. J.; Gutierrez, H. R. H.; Xiong, Q.; Pellen, M. E.; Petko, J. S.; Werner, D. H.; Eklund, P. C. Optical Antenna Effect in Semiconducting Nanowires. *Nano Lett.* **2008**, *8*, 1341–1346.
45. Wei, H.; Hao, F.; Huang, Y. Z.; Wang, W. Z.; Nordlander, P.; Xu, H. X. Polarization Dependence of Surface-Enhanced Raman Scattering in Gold Nanoparticle-Nanowire Systems. *Nano Lett.* **2008**, *8*, 2497–2502.
46. Etchegoin, P. G.; Galloway, C.; Le Ru, E. C. Polarization-Dependent Effects in Surface-Enhanced Raman Scattering (SERS). *Phys. Chem. Chem. Phys.* **2006**, *8*, 2624–2628.
47. Le Ru, E. C.; Galloway, C.; Etchegoin, P. G. On the Connection between Optical Absorption/Extinction and SERS Enhancements. *Phys. Chem. Chem. Phys.* **2006**, *8*, 3083–3087.